This is the peer-reviewed, final accepted version for American Mineralogist, published by the Mineralogical Society of America.
The published version is subject to change. Cite as Authors (Year) Title. American Mineralogist, in press.
DOI: https://doi.org/10.2138/am-2022-8187. http://www.minsocam.org/

Revision 1

Pressure-induced *C*23–*C*37 transition and compression behavior of orthorhombic Fe_2S to Earth's core pressures and high temperatures

Claire C. Zurkowski[a], Barbara Lavina[b,c], Nigel M. Brauser[a], Anne H. Davis[a], Stella Chariton[b], Sergey Tkachev[b], Eran Greenberg[b†], Vitali B. Prakapenka[b], Andrew J. Campbell[a]

[a]University of Chicago, Department of the Geophysical Sciences, 5734 S Ellis Ave, Chicago, IL 60637, USA
[b]Center for Advanced Radiation Sources, University of Chicago, Chicago, IL 60637, USA
[c]X-ray Science Division, Advanced Photon Source, Argonne National Laboratory, Argonne, IL 60439, USA
[†]Now at Applied Physics Department, Soreq Nuclear Research Center (NRC), Yavne 81800, Israel

Corresponding Author: Claire Zurkowski, czurkowski@uchicago.edu

Highlights

- Fe_2S is observed coexisting with iron between 25 and 194 GPa and to 2500 K.
- A pressure-induced *C*23–*C*37 Fe_2S phase transition is observed at core mantle boundary pressures.
- The density profile of *C*37 Fe_2S indicates that 8.6 wt% S is required to match the density at Earth's inner core boundary.

ABSTRACT

The phase stability of orthorhombic Fe_2S was explored to 194 GPa and 2500 K using powder and multigrain synchrotron X-ray diffraction techniques. Between 30 and 120 GPa, a *C*23-like (Co_2P, *Pnma*, *Z*=4) Fe_2S unit cell is observed and determined to exhibit a highly compressible *a* axis. A softening of the *a* axis occurs between 120 and 150 GPa and a relative stiffening of the *b* and *c* axes accompanies this compressibility change. Above 150 GPa, the *a* axis stiffens as the *b* and *c* axes soften and a *C*37-like (Co_2Si, *Pnma*, *Z*=4) Fe_2S unit cell is measured. On the basis of these changes in unit-cell geometry, a pressure-induced *C*23–*C*37 Fe_2S phase transition is inferred between 120–150 GPa. The *C*23 and *C*37 (*Pnma, Z*=4) structures are closely related and share the same site symmetries. Forming the *C*37 structure from the *C*23 structure requires a shortening of the *a* axis and lengthening of the *b* and *c* axes

accompanied by a 4- to 5-fold coordination change. The softening of the *a* axis above 120 GPa may therefore indicate the onset of a coordination change, and the final compressibility change above 150 GPa may mark the completion of this phase transition. The presented pressure-temperature (*P-T*) stabilities of *C*23 and *C*37 structures of Fe_2S are in agreement with and resolve the differing observations of two previous studies (Tateno et al. 2019; Zurkowski et al. in press). As *C*37 Fe_2S is observed to core-mantle boundary pressures and high temperatures, the *C*37 Fe_2S density profile through Earth's outer core was determined by fitting the *C*23 Fe_2S equation of state (<120 GPa) and applying a 1.6 % volume reduction based on the *C*37 Fe_2S volume residuals to this fit. Comparing the density of liquid *C*37 Fe_2S with that of liquid hcp-Fe (Dewaele et al. 2006) and the seismologically determined density deficit of Earth's core (Irving et al. 2018), 13.9±1.5 wt% and 8.6±0.8 wt% sulfur is required to match the density at the CMB and ICB, respectively, for a purely Fe–S core.

INTRODUCTION

Earth's seismologically determined density profile and geomagnetic field indicate that its core is likely iron rich, and chemical analysis of mantle materials compared to meteorite compositions suggest that the density deficit measured in Earth's core compared to iron is a result of a light element component (e.g. Birch, 1952; Jephcoat and Olsen, 1987; McDonough and Sun, 1995; Scott and Wasson, 1975). Earth's core is a complex, natural system, and cosmochemically abundant elements such as S, O, Si, C and H are primary core alloying candidates. Investigating the densities of these core-relevant Fe-alloys at high pressures and temperatures is critical for assessing the multicomponent composition of Earth's liquid outer and solid inner core (Birch, 1952, McDonough and Sun, 1995). Fe–S alloys are of particular

55 importance because sulfur is a significant component of the iron-rich meteorites thought to
56 originate in the cores of planetesimals. As Earth likely formed from collision and aggregation of
57 planetesimals, iron meteorites may be relict of the building blocks of terrestrial planets like
58 Earth. Sulfur also significantly lowers the melting point of pure iron (e.g. Campbell et al. 2007;
59 Chen et al. 2008; Fei et al. 1997; Fei et al. 2000; Morard et al. 2008), and during Earth's
60 differentiation, the presence of sulfur would have facilitated metal melt formation and core
61 segregation (e.g. Murthy and Hall, 1970; Shannon and Agee, 1996; Stevenson, 1988; Yoshino et
62 al. 2003).

63 The Fe–S system is characterized by intricate phase and melting relations. Several high
64 *P-T* sulfide phases have been reported in Fe-rich systems. At low pressures, Fe and FeS form a
65 binary eutectic with Fe_3S_2 stabilizing as an intermediate compound above 14 GPa. Fe_3S_2 melts at
66 a peritectic to FeS plus liquid at 14 GPa (Fei et al. 1997), and a non-ideal Fe-rich liquidus curve
67 is observed between 14 and 21 GPa (Chen et al. 2008; Tao and Fei, 2021). Above 21 GPa,
68 several other sulfides have been identified: Fe_3S is observed to melt incongruently to Fe_3S_2 plus
69 liquid, and Fe_2S is observed over a limited subsolidus temperature and composition range (Fei et
70 al. 2000). The structures of Fe_3S_2 (exhibiting nonstoichiometry close to $Fe_{3.2}S_2$) and Fe_2S were
71 preliminarily investigated by TEM after synthesis at 21 GPa and 1900 K and were reported to
72 both adopt hexagonal lattices (Koch-Müller et al. 2002). Fe_3S adopts a tetragonal unit cell with
73 the Fe_3P-type structure (*I*-4, *Z*=8) is reported to be the Fe-rich sulfide to 250 GPa at high
74 temperatures (Fei et al. 2000; Kamada et al. 2010; Mori et al. 2017; Ozawa et al. 2013; Seagle et
75 al. 2006; Thompson et al. 2020). Above 250 GPa, tetragonal Fe_3S breaks down into *B*8 FeS+Fe
76 at moderate temperatures, and at high temperatures above 250 GPa, *B*8 FeS and Fe react to form
77 an orthorhombic Fe_2S on the liquidus in Fe-rich compositions (Mori et al. 2017; Ozawa et al.

2013; Tateno et al. 2019). The orthorhombic Fe_2S observed at these conditions adopts a unit-cell compatible with the *C*37 structure (Co_2Si-type, *Pnma*, *Z*=4) (Tateno et al. 2019).

As Fe_2S is observed coexisting with Fe on the liquidus at pressures related to Earth's outer core (136–360 GPa), investigating its material properties has become the focus of recent investigations (Tateno et al. 2019; Zurkowski et al. in press). Tateno et al. (2019) measured the volume of Fe_2S between 190 and 306 GPa and determined that its unit-cell parameters and diffraction angles are compatible with an orthorhombic lattice with space group *Pnma.* In particular, the *c*/*a* ratio measured for Fe_2S is similar to that of the Co_2Si structure type (*C*37, *Pnma*, *Z*=4) (Geller and Wolontis, 1955) (Figure 1). The recent crystallographic analyses of Fe_2S synthesized at ~90 GPa and 2400 K established that Fe_2S assumes a *C*23 structure at these conditions (Co_2P-type, *Pnma*, *Z*=4) (Zurkowski et al. in press) (Figure 1). To resolve the differences in observations between these two recent studies, a *C*23–*C*37 transition in Fe_2S must occur in the 90–190 GPa pressure range. Furthermore, A *C*23–*C*37 pressure-induced transition has been recently reported in Fe_2P around 42 GPa (Nakajima et al. 2020), supporting that pressure plays a role in shaping the Co_2P structure type into the Co_2Si structure type, as the Fe–P system has been shown to be a low-pressure analog to the Fe–S system (e.g. Gu et al. 2016).

Comparing the *C*23 and *C*37 structures may provide insight into the plausible mechanism for a pressure-induced *C*23–*C*37 transition. These structures are routinely compared on the basis of their relative unit cells and coordination environments (e.g. Rundqvist 1960; Shoemaker and Shoemaker, 1965; Rundqvist and Nawapong, 1966; Jeitschko and Altymeyer, 1990; Nakajima et al. 2020). The *C*23 and *C*37 structures have the same site symmetries, space group, and formula units per cell, but the *C*37 structure is distinct from the *C*23 structure based on its relatively larger *b* and *c* axes and shorter *a* axis (Figure 1). The *C*23 structure is composed of MX_4

tetrahedra and MX_5 square pyramids while the *C*37 structure is composed of MX_5 dipyramids and MX_5 square pyramids (Figure 1). The additional *M–X* bond in the *C*37 MX_5 dipyramid compared to the *C*23 MX_4 tetrahedra is oriented along the *a* direction. The *C*37 structure can therefore be seen as a distortion of the *C*23 structure: the *C*37 structure forms from the *C*23 structure by shortening the *a* axis and lengthening the *b* and *c* axes, resulting in a 4- to 5-fold coordination change with the next nearest *X* site along the *a* direction.

This work investigates the compression behavior of orthorhombic Fe_2S using powder and multigrain X-ray diffraction techniques between 29 and 194 GPa and to 2500 K. A *C*23-like Fe_2S phase is observed between 30 and 120 GPa and at high temperatures. Between 120 and 150 GPa, a softening of the *a* axis and relative stiffening of the *b* and *c* axes is measured, and, above 150 GPa, a *C*37-like unit-cell of Fe_2S is observed. A sharp *C*23–*C*37 transition is not observed; instead, the *C*23 Fe_2S unit-cell evolves towards a *C*37 structure with pressure and this behavior intensifies in the 120-150 GPa pressure range, likely as a result of the onset of a 4- to 5-fold coordination change on the FeS_4 tetrahedral sites. Fe_2S is observed in this study to coexist with hcp-Fe, and, as the *C*23–*C*37 Fe_2S transition occurs around core-mantle boundary pressures and high temperatures, this transition in Fe_2S is important to consider in the context of Earth's core chemistry and dynamics. A thermal equation of state (EoS) is presented for *C*23 Fe_2S to 120 GPa and a volume reduction is applied to characterize the *P-V-T* behavior of *C*37 Fe_2S above 150 GPa. Comparing the calculated density of *C*37 Fe_2S with that of hcp-Fe (Dewaele et al. 2006) and the seismologically determined densities at CMB and ICB conditions (Dziewonski and Anderson, 1981; Irving et al. 2018), the sulfur content of a purely Fe–S core is presented.

MATERIALS AND METHODS

In this study, Fe_2S was observed in experiments on Fe-rich Fe–S and also Fe–S–O compositions. Previous single crystal analyses of Fe_2S at 90 GPa and 2400 K (Zurkowski et al. in press) indicate that Fe_2S forms in an oxygen-free system with all sites occupied by sulfur. Observations of Fe_2S in FeO saturated compositions are therefore included in this study, as differences in measured Fe_2S volumes are not discernable between the Fe–S and Fe–S–O compositions. Starting powders for these experiments consisted of Fe (99.9+%, <10μm, Alfa Aesar), iron sulfide (FeS, 99.99%, Alfa Aesar) and iron oxide (FeO, 99.5%, Alfa Aesar) powders. Two Fe-FeS compositions were weighed: Fe–12.5S, Fe–23S (dashed notation indicates wt%). The Fe-FeS compositions were homogenized in a mortar and pestle for 1 hour in alcohol, dried and then mixed dry for a short duration to reset any density settling during alcohol evaporation. Fe-S-O mixtures were homogenized in alcohol in a ball mill for 1.5-3 hours at 20 Hz, dried and then ball milled dry for a short duration to reset any density segregation. The final Fe–S–O starting compositions were measured by SEM: Fe–13S–5O, Fe–17S–5O, Fe–6S–12O, Fe–3O–7S, and Fe– 4O–8S.

The starting material was compressed into foils between two ungasketed diamond anvils prior to loading into the diamond anvil cell (DAC). Type I diamonds and tungsten carbide or cBN seats as well as Boehler-Almax conical diamonds and seats were used for the high-pressure experiments. The culet sizes ranged from 300-50 μm. Sample foils were loaded into rhenium gaskets preindented to 28-40 GPa with 120-25 μm diameter sample chambers. Samples were loaded in KCl, KBr, NaCl, SiO_2, or Ne pressure media and were dried at 100ºC for 30 minutes prior to gas loading or pressurization.

147 Angle dispersive X-ray diffraction (XRD) experiments took place at Argonne National
148 Laboratory, Sector 13 ID-D (GeoSoilEnviroCars) of the Advanced Photon Source. Data was
149 collected with a 2 μm x 3 μm full width at half maximum incident X-ray beam with energy of 37
150 or 42 keV. Diffracted X-rays were collected using a CdTe 1M Pilatus detector or a MarCCD
151 detector with a typical exposure time of 1-2 s. The sample to detector geometry was calibrated
152 using the diffraction of LaB_6 NIST standard at 1 bar.

153 Double-sided laser heating was conducted using fiber lasers shaped with a flat top ~10 μm
154 radius spot size. The X-ray beam and laser were aligned using the X-ray induced fluorescence of
155 the alkali halide pressure media and sample, ruby or the gasket (Prakapenka et al. 2008).
156 Temperature was measured spectroradiometrically (Heinz and Jeanloz, 1987) during XRD
157 collection using a gray body approximation of the thermal emission from a 6 μm diameter region
158 at the center of the laser heated spot. A 3% correction was applied to account for axial
159 temperature gradients through the sample (Campbell et al. 2007; 2009). Samples were typically
160 heated for 15-30 minutes.

161 Rotational scans of the sample chamber were collected upon quench during select
162 experiments. Upon quenching from target temperatures, rotation XRD images were collected
163 spanning ±17 to ±30º depending on the angular opening of the cell. During rotation, diffraction
164 images were collected in 0.25º-0.5º steps with exposure times of 1–2 s at each step. Grains of the
165 target Fe_2S phase were then identified in reciprocal space (Rigaku OD, 2018).

166 Powder diffraction data were integrated using Dioptas (Prescher and Prakapenka, 2015).
167 Peaks were fitted using Fityk (Wojdyr, 2010) and lattice parameters from each measurement
168 were obtained on the basis of an orthorhombic Fe_2S cell. For runs where rotational scans were

169 performed, data from individual grains of Fe_2S were indexed using Crysalis Pro (Rigaku OD,
170 2018).

171 ## RESULTS AND DISCUSSION

172 ### Evidence for a *C*23–*C*37 transition in Fe_2S

173 Between 30 and 194 GPa and upon heating to subsolidus temperatures, in all
174 compositions examined, hcp-Fe (and FeO, if oxygen was present) was observed in the diffraction
175 patterns coexisting with a set of diffraction angles that cannot be accounted for by the tetragonal
176 Fe_3S phase that is reported to be stable at higher temperatures in this pressure range (e.g. Ozawa
177 et al. 2013; Seagle et al. 2006; Thompson et al. 2020) (Figure 2). The peaks were instead indexed
178 to an orthorhombic lattice with a volume equal to 4 formula units of Fe_2S. As shown in the
179 example provided in Figure 2a, the diffraction angles measured for Fe_2S at 74(1) GPa and
180 1750(110) K fit to an orthorhombic unit-cell with parameters: a = 5.253(2)Å, b = 3.328(2) Å,
181 and c = 6.222(3) Å. This cell is compatible with that reported for *C*23 Fe_2S at 90 GPa
182 (Zurkowski et al. in press). In contrast, at 169(1) GPa and 2100(120) K (Figure 2b), Fe_2S is
183 observed with unit cell parameters: a = 4.561(3) Å, b = 3.281(3) Å, and c = 6.145(5) Å, in
184 agreement with the *C*37-like Fe_2S unit-cell geometry reported by Tateno et al. (2019) at ~190
185 GPa.

186 The high temperature observations of Fe_2S in *P-T* space are shown in Figure 3 and all data
187 associated with these measurements are given in Appendix A1. The light blue data indicate the
188 stability of a *C*23-like Fe_2S, including the data from Zurkowski et al. (in press), and the emerald
189 green data indicate the stability of *C*37 Fe_2S, including the data from Tateno et al. (2019). The

split blue-green data points represent the region where the measured Fe_2S unit-cell is transitional between the *C*23 and *C*37 structures. The observed *C*23 and *C*37 unit cells suggest that the structural evolution of Fe_2S is more sensitive to pressure than temperature (Figure 3).

The *C*23, transitional, and *C*37 Fe_2S phase fields plotted in Figure 3 were determined based on the evolution of the measured unit cell parameters with pressure (Figure 4, including the data by Zurkowski et al. *in press* and Tateno et al. 2019). Between 29 and 306 GPa, Fe_2S exhibits pronounced anisotropic compression, wherein the *a* axis is more compressible than the *b* and *c* axes (Figure 4a). A more rapid softening of the *a* axis and relative stiffening of the *b* and *c* axes is observed above ~120 GPa, indicating a change in compressibility of the structure. Stiffening of the *a* axis and softening of the *b* and *c* axis is further observed above ~150 GPa, marking another structural change in Fe_2S (Figure 4a). The Fe_2S unit-cell geometries reported by Zurkowski et al. (in press) and Tateno et al. (2019) support the trend observed in Figure 4a; namely a *C*23 Fe_2S cell between 30 and ~120 GPa and a *C*37 Fe_2S unit cell above ~150 GPa. Between these pressures, the unit cell geometry is transitional between the *C*23 and *C*37 lattices.

The compressional behavior of Fe_2S can also be viewed in terms of the *c*/*a* ratio trend and systematically compared to the *c*/*a* ratio of the Co_2P and Co_2Si structure types (Figure 4b). The relative unit cells of M_2X and MX_2 structures with these site symmetries have been routinely compared and grouped into Co_2P- and Co_2Si-branches of the $PbCl_2$ family in previous studies (e.g. Rundqvist 1960; Shoemaker and Shoemaker, 1965; Rundqvist and Nawapong, 1966; Jeitschko and Altymeyer, 1990; Nakajima et al. 2020). At ambient conditions, Co_2P and Co_2Si have *c*/*a* ratios of 1.19 and 1.44 respectively (dashed horizontal lines in Figure 4b), and here we take these values as characteristic of their two structure types and associated with the difference in their cation coordinations. Up to 112 GPa, the Fe_2S *c/a* ratio shows a nearly linear trend

increasing from around 1.14 at 29 GPa to 1.22 at 112 GPa, similar to that of the Co_2P structure type (Figure 4b). Between 159 GPa and 306 GPa, the Fe_2S *c*/*a* ratios show an approximately linearly increasing trend with *c*/*a* ratios ranging from 1.34–1.40, more like that of the Co_2Si structure type (Figure 4b). Across the pressure range of this study (30-194 GPa), the data trend along an S-shaped curve where Fe_2S is more rapidly evolving from a *C*23- to a *C*37-like unit cell in the 120–150 GPa transitional pressure range. The inflection point in this trend occurs around 142 GPa, marking the possible cut-off pressure between the *C*23 and *C*37 structural stabilities (Figure 4).

Based on the systematic comparison between the *C*23 and *C*37 structures (Figure 1), a highly compressible *a* axis and the onset of bonding between Fe and the next nearest S site along the *a* direction is necessary for a *C*23–*C*37 pressure-induced transition. The unit-cell compression of Fe_2S shown in Figure 4 demonstrates this pronounced anisotropic compression behavior. The softening of the *a* axis above 120 GPa may also indicate the onset of a coordination change, and the final compressibility change above 150 GPa may mark its completion. Further crystallographic analysis is required to better characterize the details of the Fe_2S atomic arrangement across this transition, but it is clear that Fe_2S exhibits distinct structural changes in this pressure range that are supportive of the requisite behavior of a pressure-induced *C*23–*C*37 transition.

Previous studies have reported analogous *C*23–*C*37 transitions in other M_2X compounds, including PbF_2 at 10 GPa and Fe_2P at 42 GPa (Haines et al. 1998; Nakajima et al. 2020). These lower pressure studies observe the *C*23–*C*37 M_2X transition to occur over a few GPa, whereas changes in compressibility of Fe_2S bracket a *C*23–*C*37 Fe_2S transition across ~30 GPa pressure range above 120 GPa. The difference in chemistry and the higher transition pressures observed

in Fe_2S compared to PbF_2 and Fe_2P may play a role in the difference in behavior across the transition, but further compression experiments are needed to better characterize the structural changes in these phases during the respective *C*23–*C*37 transitions.

Equation of state of *C*23 and *C*37 Fe_2S

The measured volumes of Fe_2S between 29 and 194 GPa are plotted in Figure 5 along with the Fe_2S volumes reported by Zurkowski et al. (in press) and Tateno et al. (2019) . As Fe_2S is observed to undergo a change in compressibility above 120 GPa and again above 150 GPa (Figure 4), a thermal equation of state was fit only to the *C*23 Fe_2S volumes measured below the first compressibility change (<120 GPa, Figure 4) . The *C*23 Fe_2S *P-V* data were fitted to a Mie-Grüneisen EoS given in Equation 1. The $P_{300}(V)$ term in Equation 1 (expanded in Equation 2) is a third-order Birch-Murnaghan EoS (Birch, 1952) fit to the room temperature *P-V* data via the isothermal bulk modulus, K_0; pressure derivative, K'; and zero-pressure volume, V_0. High temperature data were fitted using the Grüneisen parameter (γ, Equation 3) and the Debye model of vibrational energy relating thermal energy *E* with γ and Debye temperature (θ_D, Equation 4). To decrease the number of fitted parameters, anharmonic and electronic contributions to thermal pressure were not included, and the one bar Grüneisen parameter, γ_0, was fit to our high temperature data with θ_0 and q fixed to 400 K and 1, respectively.

1. $$P(V, T) = P_{300}(V) + (\gamma/V)[E(\theta_D, T) - E_{300}(\theta_D, 300)]$$

2. $$P_{300}(V) = 3K_0 f(1 + 2f)^{2.5} * (1 + 1.5(K' - 4) f), f = 0.5 * ((V/V_0)^{(-2/3)} - 1)$$

3. $$\gamma = \gamma_0 (V/V_0)^q$$

4. $$\theta_D = \theta_0 \, exp[\gamma_0(1 - (V/V_0)^q/q]$$

The fitted *C*23 Fe_2S equation of state is listed in Table 1 and the covariance in the EoS parameters are plotted in Figure S1. The room temperature, 1000 K, 2000 K and 3000 K isotherms calculated from this EoS fit are plotted in Figure 5. Pressure residuals for the *C*23 Fe_2S data (<120 GPa) show a root mean square value of ~1.5 GPa (Figure 5b). The pressure residuals for the Fe_2S measurements in the 120–194 GPa range (triangles, Figure 5) and those reported by Tateno et al. (2019) were calculated based on the EoS and plotted in Figure 5b. These data are not well described by the *C*23 Fe_2S equation of state, supporting the observed structural changes in Fe_2S above 120 GPa.

As *C*37 Fe_2S is only observed above 150 GPa, the low pressure data necessary for adequately describing its EoS parameters are lacking. To characterize the *P-V-T* behavior of *C*37 Fe_2S, we assume here that its compressional and thermal behavior are identical to the C23 phase, with only a different volume V_0. The high-temperature volume residuals observed for *C*37 Fe_2S above 150 GPa show an average 1.6% decrease in volume compared to the *C*23 Fe_2S thermal EoS (Figure S2). As the *C*23 and *C*37 structure types are closely related and low pressure (<150 GPa) data for *C*37 Fe_2S is not available, a *C*37 Fe_2S EoS was constructed by applying this volume change to the *C*23 Fe_2S thermal equation of state, while keeping the K_0, K', and γ_0 parameters fixed. The resulting modified thermal equation of state is plotted with the high temperature *C*37 data (>150 GPa) in Figure 6. The 120–150 GPa pressure range was not included in this volume change calculation, as a phase transition is likely occurring.

The 300 K *C*37 Fe_2S data reported in the Tateno et al. (2019) study show anomalously high volumes compared to the high temperature *C*37 Fe_2S volumes measured in this study (Figure 5). In the Tateno et al. (2019) study, Fe_2S was synthesized at high pressures and temperatures, quenched, and decompressed at 300 K in an MgO pressure medium, a significantly harder

281 medium compared to Ne or NaCl mediums used to collect the room temperature data reported in
282 this study. The greater room temperature Fe_2S volumes measured in the Tateno et al. (2019)
283 study may be a consequence of the more nonhydrostatic nature of the ceramic medium compared
284 to alkali halide and noble gas media, and future room temperature decompression measurements
285 on *C*37 Fe_2S synthesized in neon would benefit the EoS fitting presented here and resolve the
286 difference in volume of Fe_2S reported in this study compared to that of Tateno et al. (2019).
287

288 **IMPLICATIONS**

289 The *C*23–*C*37 Fe_2S transitional pressure range (120-150 GPa) encompasses core-mantle
290 boundary pressures. As Fe_2S is observed in this study coexisting with hcp-Fe at moderate
291 temperatures, further experimental work is required to understand how the *C*23–*C*37 Fe_2S
292 transition affects the thermodynamics and phase relations in Fe-rich systems at core-mantle
293 boundary conditions. Furthermore, at pressure beyond the *C*23–*C*37 transition in Fe_2S,
294 anisotropic compression of *C*37 Fe_2S is observed to still higher pressures, where the *a* axis
295 continues to compress more rapidly than the *b* and *c* axes (this study, Tateno et al. 2019). As
296 *C*37-like Fe_2S is observed in Fe-rich systems on the liquidus to at least 306 GPa (Tateno et al.
297 2019), any further structural transitions in *C*37 Fe_2S may be addressed in future experiments as
298 this phase, or a high-pressure polymorph of it, may be relevant to the thermodynamics of
299 solidification at Earth's inner core boundary.

300 To constrain the possible sulfur contribution to the density of Earth's multicomponent core,
301 the density profile of Fe_2S was calculated using the *C*37 Fe_2S EoS and extrapolated throughout
302 the core. As the *C*37 Fe_2S phase is stable at core mantle boundary pressures and high
303 temperatures, the *C*37 Fe_2S density profile extrapolated through the core provides an important

addition to previous Fe-sulfide EoS studies (e.g. Fei et al. 2000; Kamada et al. 2014; Seagle et al. 2006; Tateno et al. 2019). The densities of Fe_2S calculated at CMB and ICB conditions were then combined with that of hcp-Fe (Dewaele et al. 2006) and compared to the seismologically determined CMB density reported by Irving et al. (2018) and the ICB density reported by the PREM model (Dziewonski and Anderson, 1981). Results from the Irving et al. (2018) study of the outer core is used for the CMB density calculations in this study, as this work reported elastic parameters that better predict the observed normal mode frequencies and body wave models for the outer core. A CMB density and pressure of 10.05 g/cm^3 and 135.8 GPa (Irving et al. 2018) and an ICB density and pressure of 12.8 g/cm^3 and 328.9 GPa (Dziewonski and Anderson, 1981) was implemented into our calculations, respectively. An adiabatic temperature profile for the outer core (Birch, 1952), a 1% volume increase from solid to liquid iron alloy (Anderson, 2003), and a CMB temperature set at 4000 ± 500 K (Anderson, 2003) was assumed. The inner core boundary temperature, calculated along the hcp-Fe adiabat, was determined to be 5200 ± 500 K.

Figure 7 shows the adiabatic density profiles of *C*37 Fe_2S (this study) (blue) and hcp-Fe (Dewaele et al. 2006) (red), compared to the density profile for the outer core and inner core (Dziewonski and Anderson, 1981; Irving et al. 2018). Comparing these density trends, 13.9 ± 1.5% S is required to match CMB density and 8.6 ± 0.8 wt% S is required to match the ICB density. Previous iron sulfide equations of state studies conclude that 11-16 wt% S is required to match the density deficit at the CMB (e.g., Seagle et al. 2006; Thompson et al. 2016; Thompson et al. 2020) and 6.9 ± 0.9 wt% S is required to match the ICB density deficit (Kamada et al. 2014). Within error, the calculated CMB and ICB sulfur concentrations reported in this study are in good agreement with these previous works.

Earth's core is likely a multicomponent system with significant compositional contributions from cosmochemically abundant light elements such as S, Si, O, C, and H (McDonough 2003). From the density extrapolations presented here, it is apparent that the curvature of the liquid Fe_2S and Fe and the liquid outer core density profiles do not match, indicating that the density and sound velocities of a purely Fe–S core would not satisfy geophysical constraints. Furthermore, melting studies of the Fe-Fe_3S system report 5.7 ± 0.3 wt% S in the eutectic liquid at 250 GPa, and the eutectic liquid composition is likely more Fe-rich at ICB conditions (Mori et al. 2017; Tateno et al. 2019). Results from this work combined with that of Kamada et al. (2014) predict 6.9–8.6 wt% S to match the density at the inner core boundary, suggesting that the sulfur content of a purely Fe-S core may be on the S-rich side of the Fe-liquidus field, violating the observed presence of a denser inner core (Mori et al. 2017; Tateno et al. 2019). The novel equation of state for *C*37 Fe_2S reported here agrees with previous iron-sulfide EoS studies (e.g., Seagle et al. 2006; Thompson et al. 2016; Thompson et al. 2020; Kamada et al. 2014) and improves quantification of the density and elasticity of Fe-S alloys by presenting *P*-*V* data at outer core pressures and high temperatures. In comparison to geophysical constraints on the density, melting, and crystallization sequences of Earth's iron-rich core, this work also supports that sulfur is likely not the sole core-alloying light element, but rather a contributor to the chemistry and dynamics occurring in Earth's complex core.

ACKNOWLEDGMENTS

Portions of this work were performed at GeoSoilEnviroCARS (The University of Chicago, Sector 13), Advanced Photon Source (APS), Argonne National Laboratory. GeoSoilEnviroCARS is supported by the National Science Foundation - Earth Sciences (EAR - 1634415). This research used resources of the Advanced Photon Source, a U.S. Department of Energy (DOE) Office of Science User Facility operated for the DOE Office of Science by Argonne National Laboratory under Contract No. DE-AC02-06CH11357. Use of the COMPRES-GSECARS gas loading system was supported by COMPRES under NSF Cooperative Agreement EAR -1606856 and by GSECARS through NSF grant EAR-1634415 and DOE grant DE-FG02-94ER14466. This research used resources of the Advanced Photon Source, a U.S. Department of Energy (DOE) Office of Science User Facility operated for the DOE Office of Science by Argonne National Laboratory under Contract No. DE-AC02-06CH11357.This material is based upon work supported by a National Science Foundation Graduate Research Fellowship to C.C.Z. This work was also supported by the National Science Foundation by grant EAR-1651017 to A.J.C.

REFERENCES

Bazhanova, Z.G., Roizen, V.V., and Oganov, A.R. (2017) High-pressure behavior of the Fe-S system and composition of the Earth's inner core. Uspekhi Fizicheskih Nauk, 187, 1105–1113

Birch, F. (1952) Elasticity and constitution of the Earth's interior. Journal of Geophysical Research, 57, 227–286.

Campbell, A.J., Seagle, C.T., Heinz, D. L., Shen, G., and Prakapenka, V.B. (2007) Partial melting in the iron-sulfur system at high pressure: A synchrotron X-ray diffraction study. Physics of the Earth and Planetary Interiors, 162, 119–128.

Campbell, A.J., Danielson, L., Righter, K., Seagle, C.T., Wang, Y. and Prakapenka, V.B. (2009) High pressure effects on the iron–iron oxide and nickel–nickel oxide oxygen fugacity buffers. Earth and Planetary Science Letters, 286, 556–564.

Chen, B., Li, J. and Hauck, S.A. (2008) Non-ideal liquidus curve in the Fe-S system and Mercury's snowing core. Geophysical Research Letters, 35.

Dziewonski, A. M. and Anderson, D. L. (1981) Preliminary reference Earth model. Physics of the Earth and Planetary Interiors 25, 297–356.

Dewaele, A., Loubeyre, P., Occelli, F., Mezouar, M., Dorogokupets, P.I. and Torrent, M. (2006)

Quasihydrostatic equation of state of iron above 2 Mbar. Physical Review Letters, 97, 215504.

Fei, Y., Bertka, C.M. and Finger, L.W. (1997) High-pressure iron-sulfur compound, Fe_3S_2, and melting relations in the Fe–FeS system. Science, 275, 1621–1623.

Fei, Y., Li, J., Bertka, C.M. and Prewitt, C.T. (2000) Structure type and bulk modulus of Fe_3S, a new iron-sulfur compound. American Mineralogist, 85, 1830–1833.

Fei, Y., Ricolleau, A., Frank, M., Mibe, K., Shen, G. and Prakapenka, V. (2007) Toward an internally consistent pressure scale. Proceedings of the National Academy of Sciences, 104, 9182–9186.

Geller, S., and Wolontis, V.M. (1955) The crystal structure of Co2Si. Acta Crystallographica, 8, 83–87.

Gu, T., Fei, Y., Wu, X. and Qin, S. (2016) Phase stabilities and spin transitions of $Fe_3(S_{1-x}P_x)$ at high pressure and its implications in meteorites. American Mineralogist, 101, 205–210.

Heinz, D.L., and Jeanloz, R. (1987) Measurement of the melting curve of $Mg_{0.9}Fe_{0.1}SiO_3$ at lower mantle conditions and its geophysical implications. Journal of Geophysical Research, 92, 437–444.

Irving, J.C., Cottaar, S. and Lekic, V. (2018). Seismically determined elastic parameters for Earth's outer core. *Science advances*, 4(6)

Jephcoat, A. and Olson, P., (1987) Is the inner core of the Earth pure iron? Nature, 325, 332–335.

Kamada, S., Terasaki, H., Ohtani, E., Sakai, T., Kikegawa, T., Ohishi, Y., Hirao, N., Sata, N. and

Kondo, T. (2010) Phase relationships of the Fe–FeS system in conditions up to the Earth's outer core. Earth and Planetary Science Letters, 294, 94–100.

Koch-Müller, M., Fei, Y., Wirth, R. and Bertka, C.M. (2002) Characterization of high-pressure iron-sulfur compounds. Lunar and Planetary Science Conference, 1424.

McDonough, W.F. and Sun, S.S. (1995) The composition of the Earth. Chemical geology, 120, 223–253.

Momma, K. and Izumi, F. (2011). VESTA 3 for three-dimensional visualization of crystal, volumetric and morphology data. Journal of applied crystallography, 44, 1272–1276.

Mori, Y., Ozawa, H., Hirose, K., Sinmyo, R., Tateno, S., Morard, G. and Ohishi, Y. (2017) Melting experiments on Fe–Fe_3S system to 254 GPa. Earth and Planetary Science Letters, 464 135–141.

Morard, G., Andrault, D., Guignot, N., Sanloup, C., Mezouar, M., Petitgirard, S. and Fiquet, G., (2008) In situ determination of Fe–Fe3S phase diagram and liquid structural properties up to 65 GPa. *E*arth and Planetary Science Letters, 272, 620–626.

Murthy, V.R. and Hall, H.T. (1970) The chemical composition of the earth's core: Possibility of sulphur in the core. Physics of Earth Planetary Interiors, 2, 276–282.

Nakajima, Y., Araki, S., Kinoshita, D., Hirose, K., Tateno, S., Kawaguchi, S.I. and Hirao, N. (2020) New pressure-induced phase transition to Co_2Si-type Fe_2P. American Mineralogist, 105, 1752–1755.

Ozawa, H., Hirose, K., Suzuki, T., Ohishi, Y. and Hirao, N. (2013) Decomposition of Fe_3S above 250 GPa. Geophysical research letters, 40, 4845–4849.

Prakapenka, V.B., Kubo, A., Kuznetsov, A.Laskin, A., Shkurikhin, O., Dera, P., Rivers, M. L. and Sutton, S.R. (2008) Advanced flat top laser heating system for high pressure research

at GSECARS: application to the melting behavior of germanium. High Pressure Research, 28, 225–235.

Prescher, C., and Prakapenka, V.B. (2015) DIOPTAS: a program for reduction of two dimensional X-ray diffraction and data exploration. High Pressure Research, 35(3), 223–230.

Rigaku Oxford Diffraction (2018) CrysAlisPRO software system, ver. 1.171.39.44a Rigaku Corporation, Oxford, U.K

Rundqvist, S. (1960) The structures of Co_2P, Ru_2P and related phases. Acta Chemica. Scandinavica, 14, 1961–1979.

Rundqvist, S. and Nawapong, P.C. (1966) The crystal structure of ZrFeP and related compounds. Acta Chemica Scandinavica, 20, 2250–2254.

Scott, E.R. and Wasson, J.T. (1975) Classification and properties of iron meteorites. Reviews of Geophysics, 13, 527–546.

Seagle, C.T., Campbell, A.J., Heinz, D.L., Shen, G. and Prakapenka, V.B. (2006) Thermal equation of state of Fe_3S and implications for sulfur in Earth's core. Journal of Geophysical Research: Solid Earth, 111.

Shannon, M.C. and Agee, C.B. (1996) High pressure constraints on percolative core formation. Geophysical Research Letters, 23, 2717–2720.

Shoemaker, C.B. and Shoemaker, D.P., 1965. A ternary alloy with $PbCl_2$-type structure: TiNiSi (E). Acta Crystallographica 18, 900–905.

Stevenson, D.J. (1988) Fluid dynamics of core formation. In Topical Conference Origin of the Earth, 681, 87.

Tao, R. and Fei, Y. (2021) High-pressure experimental constraints of partitioning behavior of Si

and S at the Mercury's inner core boundary. Earth and Planetary Science Letters, 562, 116849.

Tateno, S., Ozawa, H., Hirose, K., Suzuki, T., I-Kawaguchi, S., and Hirao, N. (2019) Fe_2S: the most Fe-rich iron sulfide at the Earth's inner core pressures. Geophysical Research Letters, 46, 11,944–11,949.

Thompson, S., Komabayashi, T., Breton, H., Suehiro, S., Glazyrin, K., Pakhomova, A. and Ohishi, Y. (2020) Compression experiments to 126 GPa and 2500 K and thermal equation of state of Fe_3S: Implications for sulphur in the Earth's core. Earth and Planetary Science Letters, 534, 116080.

Wojdyr, M. (2010) Fityk: a general-purpose peak fitting program. Journal of applied crystallography, 43, 1126–1128.

Yoshino, T., Walter, M.J. and Katsura, T. (2003) Core formation in planetesimals triggered by permeable flow. Nature, 422, 154–157.

Zurkowski, C.C., Lavina, B., Chariton, S., Tkachev, S., Prakapenka V.B. and Campbell A.J., in press. The crystal structure of Fe_2S at 90 GPa based on single-crystal X-ray diffraction techniques. American Mineralogist, https://doi.org/10.2138/am-2022-7973

498
499
500
501
502
503
504
505

506 **FIGURE CAPTIONS**

507 **Figure 1.** Comparison between the a) *C*23, Co_2P-type and b) *C*37, Co_2Si type structures (Geller
508 and Wolontis, 1955; Rundvist, 1960) that are inferred in this Fe_2S study. The *C*23 structure is
509 composed of CoP_5 square pyramid (green) and CoP_4 tetrahedral (blue) building blocks. The *C*37
510 structure is composed of CoP_5 square pyramid (green) and CoP_5 dipyramid (blue) building
511 blocks. The *C*23 and *C*37 structures are closely related: both structures have the same ste
512 symmetries, are orthorhombic and adopt the *Pnma* (*Z*=4) space group. The *C*37 structure can be
513 seen as a distortion of the *C*23 structure; namely, the Co_2Si structure can be formed from the
514 Co_2P structure by shortening the *a* axis and lengthening the *b* and *c* axes and inducing a
515 coordination change from a 4-fold tetrahedral site (blue polyhedra) in Co_2P to a 5-fold dipyramid
516 site (blue polyhedra) in Co_2Si.

517

518 **Figure 2.** Integrated X-ray diffraction patterns exemplifying the observations of Fe_2S at high *P-*
519 *T.* a) At 74(1) GPa and 1750(110) K, Fe_2S is observed coexisting with hcp-Fe and *B*1 FeO in a
520 KCl medium. The Fe–12S–5O (wt%) starting composition is shown by the star in the ternary.
521 The fitted lattice parameters of Fe_2S support a *C*23 unit cell. The calculated diffraction angles
522 based on this fit are plotted as the red dashed vertical lines, and prominent peaks of *C*23 Fe_2S are
523 labeled with their corresponding Miller indices in light blue. Two low intensity unidentified

524 peaks are marked by the question mark (?) and may represent the initial peaks of the higher
525 temperature Fe_3S phase. b) At 169(1) GPa and 2100(120) K, Fe_2S is observed coexisting with
526 hcp-Fe in a SiO_2 pressure medium. The starting composition is Fe–12.5S (wt%) and given by the
527 star in the ternary. The fitted lattice parameters of Fe_2S support a *C*37-like unit cell. The
528 calculated diffraction angles based on this fit are plotted as the red dashed vertical lines and
529 prominent peaks of *C*37 Fe_2S are labeled with their corresponding Miller indices in emerald
530 green. One unidentified peak at around 17.5º 2Θ is distinguishable from the background and
531 marked by the question mark.
532
533 **Figure 3.** The phase stability of *C*23 and *C*37 Fe_2S in pressure-temperature space. The blue
534 circles indicate observations of a *C*23-like unit cell of Fe_2S in this study. The blue star at 89 GPa
535 and 2380 K refers to the single crystal study by Zurkowski et al. (in press) in which the structure
536 of Fe_2S was determined to be *C*23 after temperature quenching from these conditions. The
537 emerald circles represent observations of a *C*37-like unit cell of Fe_2S in this study. The emerald
538 squares refer to the Tateno et al. (2019) study, where a *C*37 Fe_2S unit cell was measured above
539 190 GPa. The split blue/green data between 110 and 150 GPa indicate the observations of a
540 transitional *C*23–*C*37 Fe_2S unit-cell.
541
542 **Figure 4. a)** Relative lattice parameters measured for Fe_2S in this study (circles) along with the
543 data reported by Tateno et al. (2019) (squares) and Zurkowski et al. (in press) (stars). The shaded
544 regions encompass the data that is more compatible with a Co_2P-like unit-cell (light blue
545 shading) and data more compatible with a Co_2Si-like unit-cell (green shading). The shaded
546 regions overlap where the relative lattice parameters measured along the *a* axis soften as the *b*

and *c* axes stiffen between ~110-150 GPa, indicating a potential transitional pressure range between these two structure types. The red, vertical dashed line represents this *C*23–*C*37 cut-off. **b)** *C/a* ratio measured for Fe_2S in this study (circles) along with the data reported by Tateno et al. (2019) (squares) and Zurkowski et al. (in press) (star). The horizontal dashed lines indicate the c/a ratio determined for Co_2P (light blue) (Rundqvist, 1960) and Co_2Si (emerald green) (Geller and Wolontis, 1955). The shaded regions encompass the data that is more compatible with a Co_2P-like *c/a* ratio (light blue shading) and data more compatible with a Co_2Si-like *c/a* ratio (green shading). As the c/a ratios measured evolve smoothly from Co_2P-like to Co_2Si-like, the shaded regions overlap in the potentially transitional pressure range. The inflection point in this S-shaped *c*/*a* ratio trend occurs around 142 GPa, differentiating the more *C*23-like and *C*37-like unit-cells of Fe_2S. The red, vertical dashed line represents this *C*23–*C*37 cut-off.

Figure 5. a) *P-V* data for Fe_2S (color coded for temperature) collected in this study (circles, triangles), Zurkowski et al. (in press) (stars), and Tateno et al. (2019) (squares). The 300 K (black), 1000 K (green), 2000 K (orange) and 3000 K (red) isotherms (solid lines) were calculated based on the thermal EoS fit to *C*23 Fe_2S data collected up to 120 GPa in this study and the study by Zurkowski et al. (in press) (~90 GPa, stars) (Table 1). The dashed line and label brackets the Fe_2S volumes included in the fit. The Fe_2S volumes measured above 120 GP are not included in the EoS fit as the lattice parameters indicate a change in compressibility and phase transition to the *C*37 structure. For comparison, the Bazhanova et al. (2017) calculated 300 K EoS for *Pnma* Fe_2S (dashed-dot line) is included. The shaded regions represent the pressure ranges where *C*23-like (light blue), transitional (blue green), and *C*37-like (light green) Fe_2S structures are observed. The red, vertical dashed line represents this *C*23–*C*37 cut-off determined

in Figure 4. **b)** Residuals to the EoS fit 1 are plotted with an r.m.s. of ~1.5 for the fitted *C*23 Fe_2S data (<120 GPa) (filled circles). The plotted open triangles depict the difference in pressure calculated from this EoS versus measured pressure for the Fe_2S data in the transitional and *C*37 Fe_2S pressure range. The black squares show the same comparison for the data reported by Tateno et al. (2019).

Figure 6. *P-V* data collected on *C*23 Fe_2S (<120 GPa, light blue shaded region), *C*37 Fe_2S (>150 GPa, green shaded region) and the transitional cell (120-150 GPa, blue-green shaded region) in this study up to 194 GPa and to 2500 K. The equation of state fit to the *C*23 Fe_2S data is plotted up to 120 GPa and is color coded for temperature. The *C*37 Fe_2S volume residuals for this equation of state show an average 1.6% volume reduction in Fe_2S above 150 GPa. This volume reduction was applied to the *C*23 Fe_2S equation of state, keeping K_0, K', and γ_0 fixed, and plotted above 150 GPa. The overlap in the *C*23 (blue) and *C*37 (green) shaded regions in the 120-150 GPa pressure range indicates the pressure range where *C*23-like Fe_2S transitions to the *C*37-like structure. This pressure range was not included in the volume reduction calculation. The red, vertical dashed line represents the *C*23–*C*37 cut-off determined in Figure 4.

Figure 7. Calculated adiabatic density curves for liquid *C*37 Fe_2S (blue) and liquid hcp-Fe (red) (Dewaele et al. 2006) plotted with the density profiles of the outer core based on the PREM model (Dziewonski and Anderson, 1981) (solid black line) and Irving et al. (2018) (dashed black line).

This is the peer-reviewed, final accepted version for American Mineralogist, published by the Mineralogical Society of America.
The published version is subject to change. Cite as Authors (Year) Title. American Mineralogist, in press.
DOI: https://doi.org/10.2138/am-2022-8187. http://www.minsocam.org/

TABLES

Table 1. EoS parameters for Fe_2S calculated based on the volumes measured in this study.

V_0 (cm3/mol)	K_0 (GPa)	K'	γ_0	q	θ_0 (K)	*Dataset*
20.6(3)	138(22)	5.6(7)	2.59(8)	1	400	***C*23 Fe_2S EoS** fitted to the *C*23 Fe_2S volumes measured in this study (< 120 GPa) and combined with the Fe_2S data from Zurkowski et al. 2021

This is the peer-reviewed, final accepted version for American Mineralogist, published by the Mineralogical Society of America.
The published version is subject to change. Cite as Authors (Year) Title. American Mineralogist, in press.
DOI: https://doi.org/10.2138/am-2022-8187. http://www.minsocam.org/

615

616

FIGURES

Figure 1, Revision 1

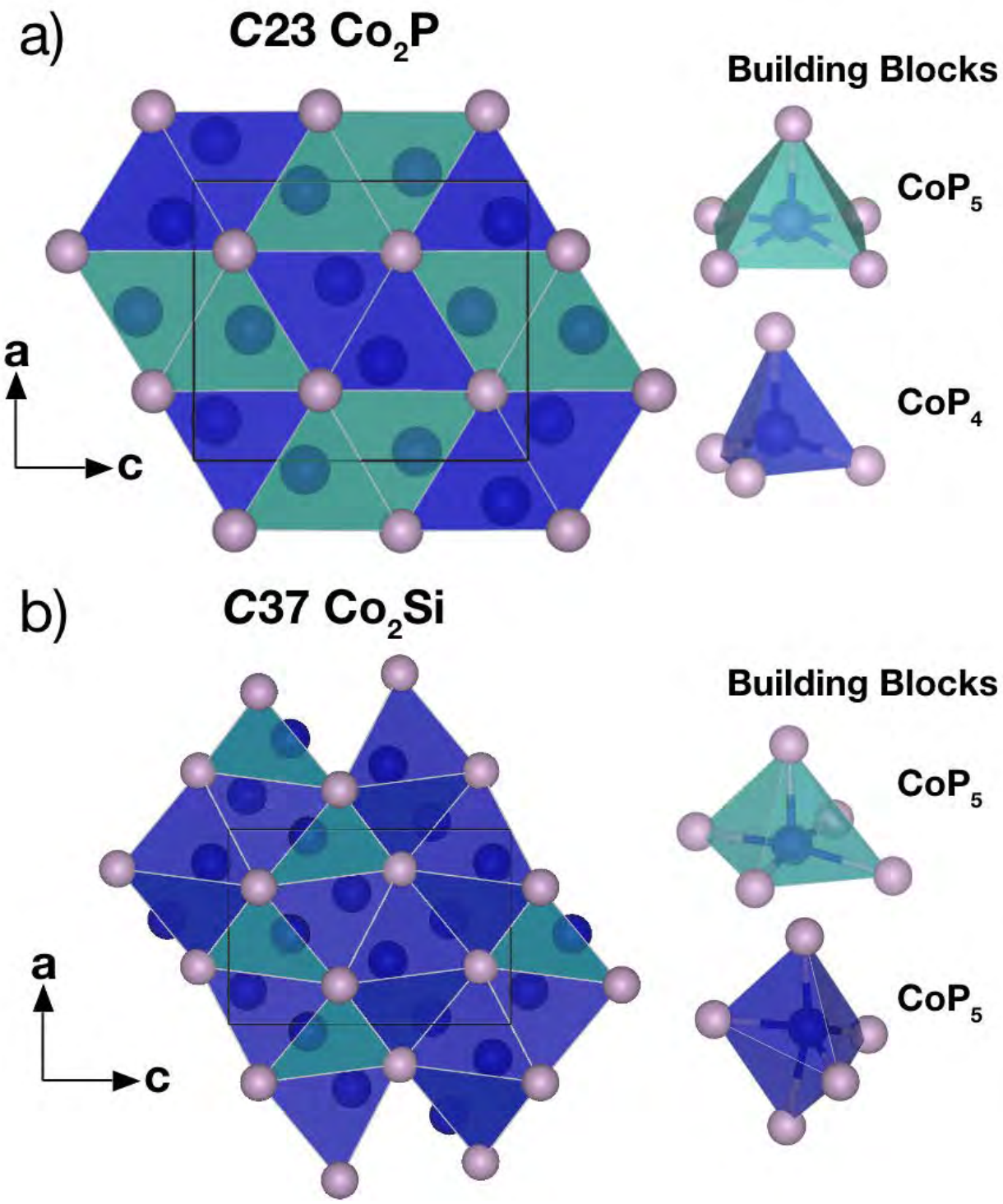

617

This is the peer-reviewed, final accepted version for American Mineralogist, published by the Mineralogical Society of America.
The published version is subject to change. Cite as Authors (Year) Title. American Mineralogist, in press.
DOI: https://doi.org/10.2138/am-2022-8187. http://www.minsocam.org/

Revision 1

Figure 2, Revision 1

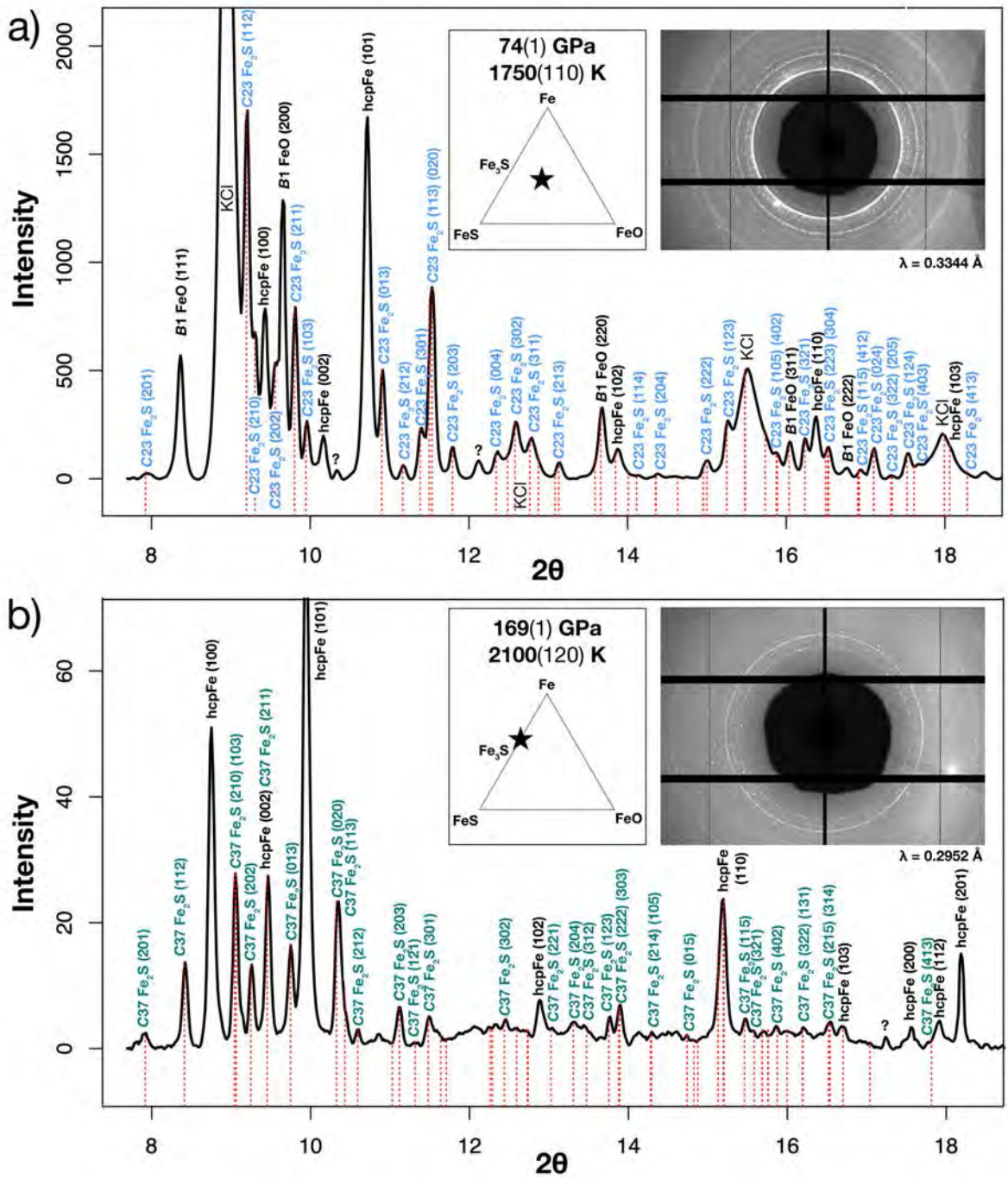

This is the peer-reviewed, final accepted version for American Mineralogist, published by the Mineralogical Society of America.
The published version is subject to change. Cite as Authors (Year) Title. American Mineralogist, in press.
DOI: https://doi.org/10.2138/am-2022-8187. http://www.minsocam.org/

Revision 1

Figure 3, Revision 1

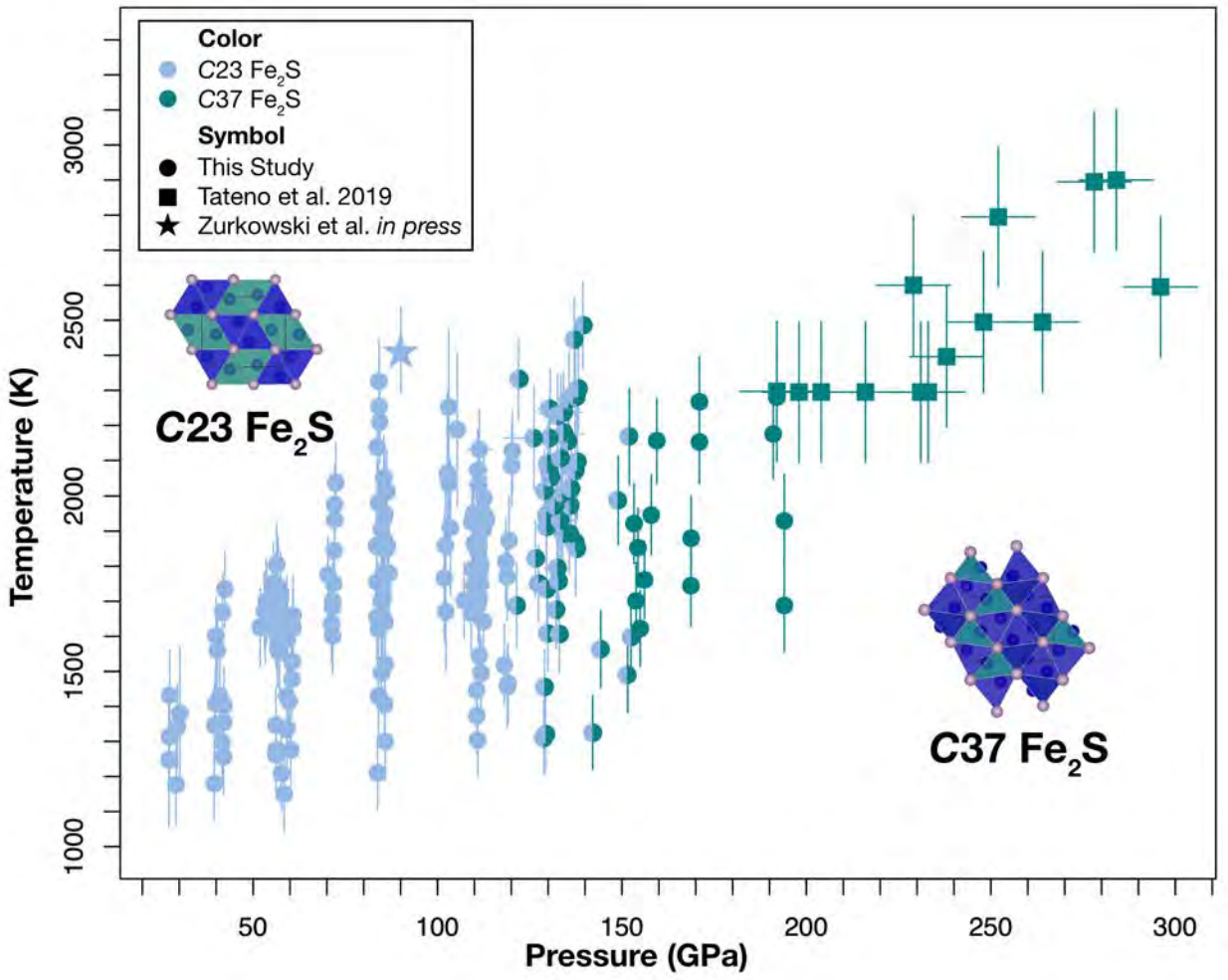

This is the peer-reviewed, final accepted version for American Mineralogist, published by the Mineralogical Society of America.
The published version is subject to change. Cite as Authors (Year) Title. American Mineralogist, in press.
DOI: https://doi.org/10.2138/am-2022-8187. http://www.minsocam.org/

Figure 4, Revision 1

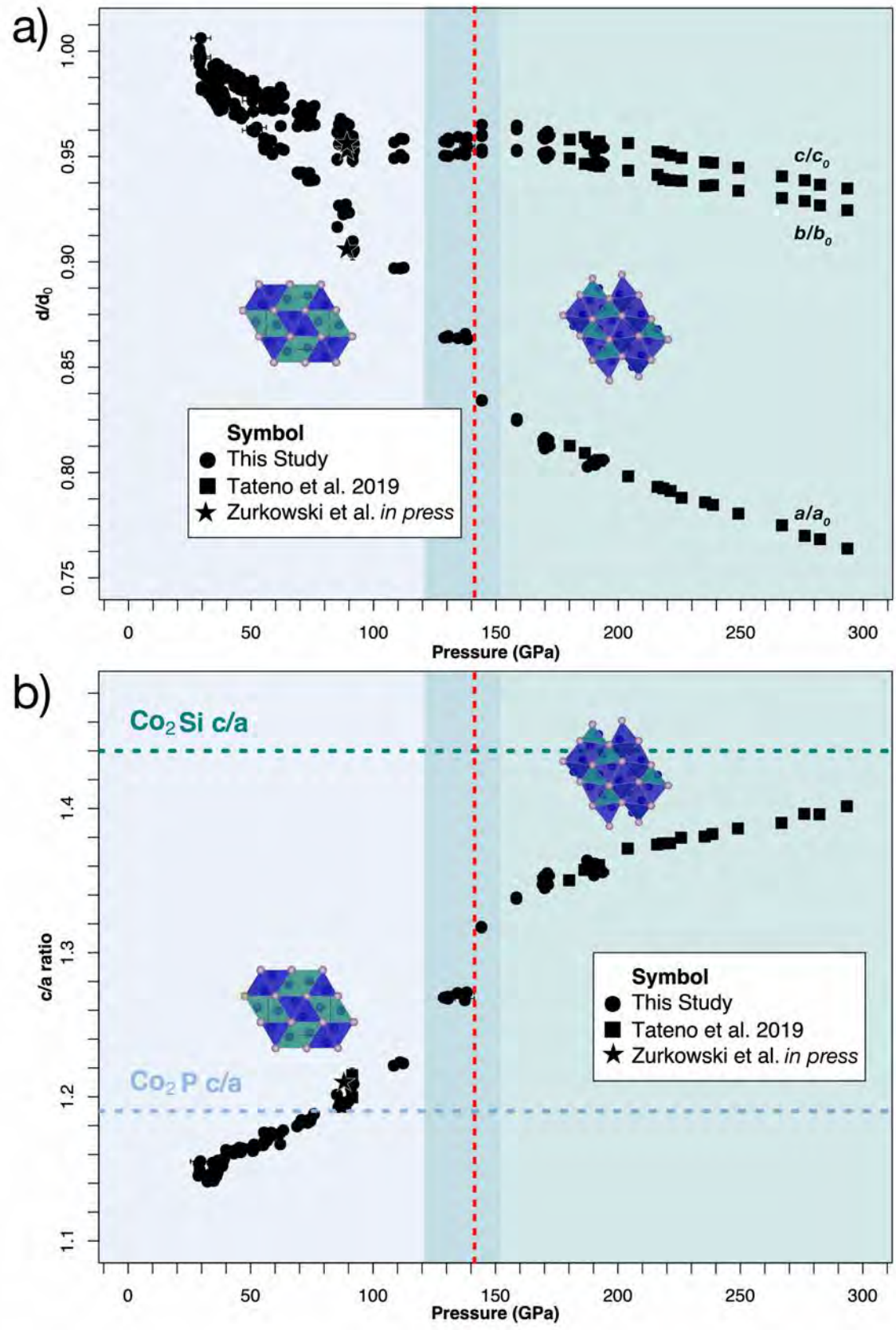

638

This is the peer-reviewed, final accepted version for American Mineralogist, published by the Mineralogical Society of America.
The published version is subject to change. Cite as Authors (Year) Title. American Mineralogist, in press.
DOI: https://doi.org/10.2138/am-2022-8187. http://www.minsocam.org/

Figure 5, Revision 1

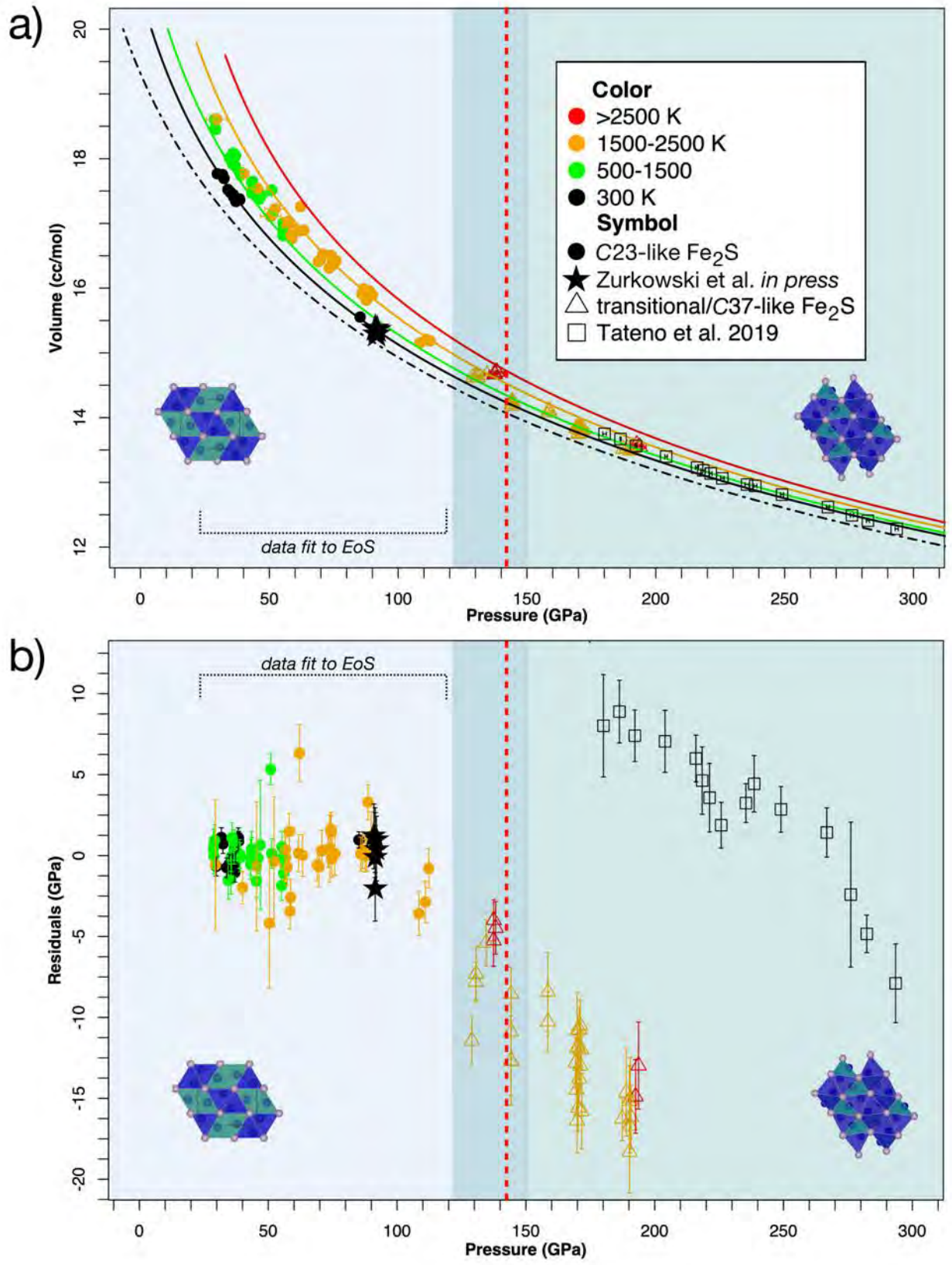

639

This is the peer-reviewed, final accepted version for American Mineralogist, published by the Mineralogical Society of America.
The published version is subject to change. Cite as Authors (Year) Title. American Mineralogist, in press.
DOI: https://doi.org/10.2138/am-2022-8187. http://www.minsocam.org/

Revision 1

Figure 6, Revision 1

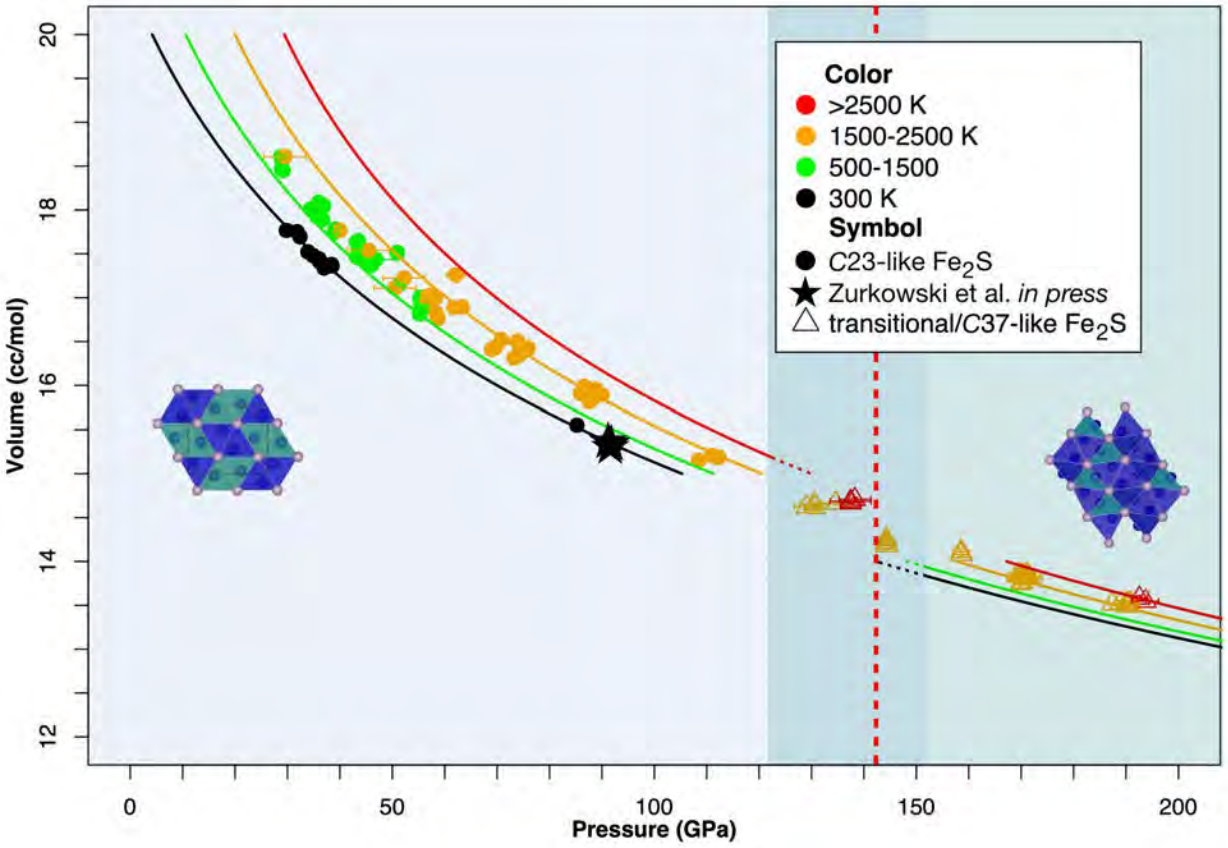

640
641

This is the peer-reviewed, final accepted version for American Mineralogist, published by the Mineralogical Society of America.
The published version is subject to change. Cite as Authors (Year) Title. American Mineralogist, in press.
DOI: https://doi.org/10.2138/am-2022-8187. http://www.minsocam.org/

642

Figure 7, Revision 1

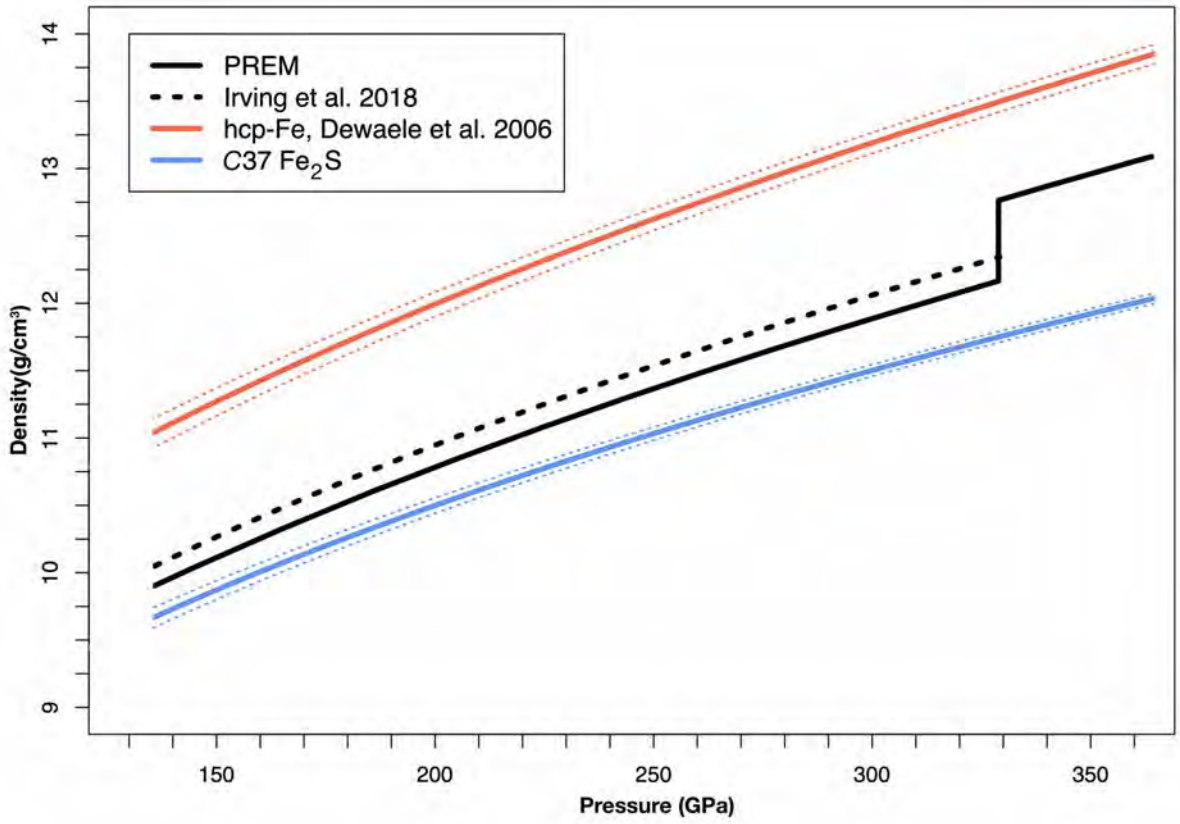

643
644
645
646
647
648
649
650
651
652
653
654
655
656
657
658
659
660
661